



1 **WRF-ELM v1.0: a Regional Climate Model to Study Atmosphere-Land Interactions Over**  
2 **Heterogeneous Land Use Regions**

3

4 Huilin Huang<sup>1\*</sup>, Yun Qian<sup>1\*</sup>, Gautam Bisht<sup>1</sup>, Jiali Wang<sup>2</sup>, Tirthankar Chakraborty<sup>1</sup>, Dalei Hao<sup>1</sup>, Jianfeng Li<sup>1</sup>,  
5 Travis Thurber<sup>1</sup>, Balwinder Singh<sup>1</sup>, Zhao Yang<sup>1</sup>, Ye Liu<sup>1</sup>, Pengfei Xue<sup>2,3</sup>, William J. Sacks<sup>4</sup>, Ethan Coon<sup>5</sup>,  
6 and Robert Hetland<sup>1</sup>

7

8 1. Atmospheric, Climate, and Earth Sciences Division, Pacific Northwest National Laboratory, Richland,  
9 WA, USA

10 2. Environmental Science Division, Argonne National Laboratory, Lemont, IL, USA.

11 3. Great Lakes Research Center, Michigan Technology University, Houghton, MI, USA.

12 4. Climate & Global Dynamics Lab, NSF National Center for Atmospheric Research, CO, USA

13 5. Climate Change Science Institute, Oak Ridge National Laboratory, TN, USA

14

15

16 Corresponding to: Huilin Huang ([huilin.huang@pnnl.gov](mailto:huilin.huang@pnnl.gov)) and Yun Qian ([yun.qian@pnnl.gov](mailto:yun.qian@pnnl.gov))

17

18

19

20

21



## 22 **Abstract**

23           The Energy Exascale Earth System Model (E3SM) Land Model (ELM) is a state-of-the-art land  
24 surface model that simulates the intricate interactions between the terrestrial land surface and other  
25 components of the Earth system. Originating from the Community Land Model (CLM) version 4.5, ELM  
26 has been under active development, with added new features and functionality, including plant hydraulics,  
27 radiation-topography interaction, subsurface multiphase flow, and more explicit land use and management  
28 practices. This study integrates ELM v2.1 with the Weather Research and Forecasting (WRF) Model  
29 through a modified Lightweight Infrastructure for Land Atmosphere Coupling (LILAC) framework,  
30 enabling affordable high-resolution regional modeling by leveraging ELM's innovative features alongside  
31 WRF's diverse atmospheric parameterization options. This framework includes a top-level driver for  
32 variable communication between WRF and ELM and Earth System Modeling Framework (ESMF) caps for  
33 WRF atmospheric component and ELM workflow control, encompassing initialization, execution, and  
34 finalization. Importantly, this LILAC-ESMF framework demonstrates a more modular approach compared  
35 to previous coupling efforts between WRF and land surface models. It maintains the integrity of the ELM's  
36 source code structure and facilitates the transfer of future developments in ELM to WRF-ELM.

37           To test the ability of the coupled model in capturing land-atmosphere interactions over regions with  
38 a variety of land uses and land covers, we conducted high-resolution (4 km) WRF-ELM ensemble  
39 simulations over the Great Lakes Region (GLR) in the summer of 2018 and systematically compared the  
40 results against observations, reanalysis data, and WRF-CTSM (WRF-coupled with the Community  
41 Terrestrial Systems Model). In general, the coupled WRF-ELM model has reasonably captured the spatial  
42 distribution of surface state variables and fluxes across the GLR, particularly over the natural vegetation  
43 areas. The evaluation results provide a baseline reference for further improvements of ELM in the regional  
44 application of high-resolution weather and climate predictions. Our work serves as an example to the model  
45 development community for expanding an advanced land surface model's capability to represent fully-  
46 coupled land-atmosphere interactions at fine spatial scales. The development and release of WRF-ELM  
47 marks a significant advancement for the ELM user community, providing opportunities for fine-scale

<https://doi.org/10.5194/egusphere-2024-1555>

Preprint. Discussion started: 20 June 2024

© Author(s) 2024. CC BY 4.0 License.



48 regional representation, parameter calibration in coupled mode, and examination of new schemes with

49 atmospheric feedback.



## 50 **1. Introduction**

51 Land surface models (LSMs) solve the exchange of water, energy, and carbon fluxes between the  
52 land surface and atmosphere (Fisher and Koven, 2020), and are frequently used to simulate response of the  
53 Earth's surface to both anthropogenic and natural forcings (Best et al., 2015). These models describe  
54 biogeophysical properties like surface roughness, albedo, and evapotranspiration efficiency, characteristics  
55 crucial for modeling the land's influence on meteorological processes (Xue et al., 1991; Dai et al., 2003;  
56 Dickinson, 1984; Sellers et al., 1986). Originally developed to support weather and climate modeling, LSMs  
57 were designed to provide essential lower boundary conditions such as radiation, energy, and water fluxes  
58 to the atmosphere.

59 Over time, LSMs have evolved significantly, with representations of increasingly complex  
60 processes that impact land surface dynamics and belowground processes, with their feedback to the  
61 atmosphere being incrementally added in newer-generation LSMs. As a consequence of all these  
62 advancements, the applicability and scope of LSMs has broadened substantially from their initial versions,  
63 introducing sophisticated representations of plant hydraulics (Fang et al., 2022; Xu et al., 2023), wildfire  
64 (Thonicke et al., 2010; Li et al., 2012; Huang et al., 2020a; Huang et al., 2021), soil biogeochemistry and  
65 nutrient cycling (Li et al., 1992; Parton et al., 1988; Jenkinson, 1990), dynamic vegetation distributions  
66 (Martín Belda et al., 2022; Weng et al., 2015; Fisher et al., 2015; Liu et al., 2019), radiation-topography  
67 interaction (Hao et al., 2021), urban-scale processes (Oleson and Feddema, 2020; Krayenhoff et al., 2020),  
68 subsurface multiphase flow (Bisht et al., 2017; Qiu et al., 2024), and land use and management (Huang et  
69 al., 2020b; Binsted et al., 2022; Calvin et al., 2019). These improvements not only advance the capability  
70 of LSMs to model complex environmental interactions but also facilitate a mechanistic understanding of  
71 changes in land-atmosphere interactions under varying environmental conditions. Particularly, they can be  
72 used to predict the disturbance of the land surface, for example, Earth's ecosystem and surface hydrology,  
73 in response to climate change and to quantify the respective biogeophysical and biogeochemical feedbacks  
74 to the climate system (Ban-Weiss et al., 2011; Fisher and Koven, 2020).



75           Recent advancements in LSMs have broad applications in land-only simulations and within global  
76 climate models (GCMs) to capture the complex interactions surrounding global climate change (Lawrence  
77 et al., 2019; Martín Belda et al., 2022; Wiltshire et al., 2020). However, the application within GCMs does  
78 not allow for the representation of land processes at kilometer scales and extreme events occurring at daily  
79 to weekly scales (such as extreme precipitation and flash drought), which are more relevant to human  
80 society. While regional refinement may appear to be a feasible solution, the associated computational costs  
81 restrict their wide adoption within the weather and climate modeling community. Alternatively, combining  
82 advanced LSMs with Regional Climate Models (RCMs) could facilitate more in-depth examinations of the  
83 climate change impacts on land surfaces and the resulting feedback at scales that have greater relevance to  
84 human society.

85           The U.S. Department of Energy’s Energy Exascale Earth System Model (E3SM) Land Model  
86 (ELM) is an advanced LSM that simulates the exchanges between terrestrial land surfaces and other Earth  
87 system components, enabling us to understand hydrologic cycles, biogeophysics, and the dynamics of  
88 terrestrial ecosystems (Burrows et al., 2020). The Weather Research and Forecasting (WRF) model serves  
89 as an essential tool widely used for regional weather prediction and climate change analysis (Skamarock  
90 and Klemp, 2008). WRF can be run with various LSMs such as Noah, Noah-MP, SSiB, CLM4. It has also  
91 been coupled with CTSM recently (CTSM Development Team, 2024; Ucar, 2020). However, integrating  
92 ELM with WRF enables comprehensive representation of land processes, following recent advancements  
93 in ELM, for more computationally efficient regional modeling applications. For instance, leaf to canopy  
94 upscaling through a two-big-leaf parameterization in ELM enables simulation of the diffuse radiation  
95 fertilization effect (Chakraborty et al., 2022a), and thus better estimates of surface water and carbon budget,  
96 a feature not present in Noah. As another example, ELM incorporates gridwise surface properties such as  
97 leaf area index (LAI), displacement height, and vegetation top and bottom height. In contrast, Noah and its  
98 variants use lookup tables with these properties prescribed for each land cover class, limiting their ability  
99 to capture spatial heterogeneity in surface properties within individual land cover types. Moreover, ELM  
100 simulations at ~km resolution highlight the significance of considering radiation-topography interaction in



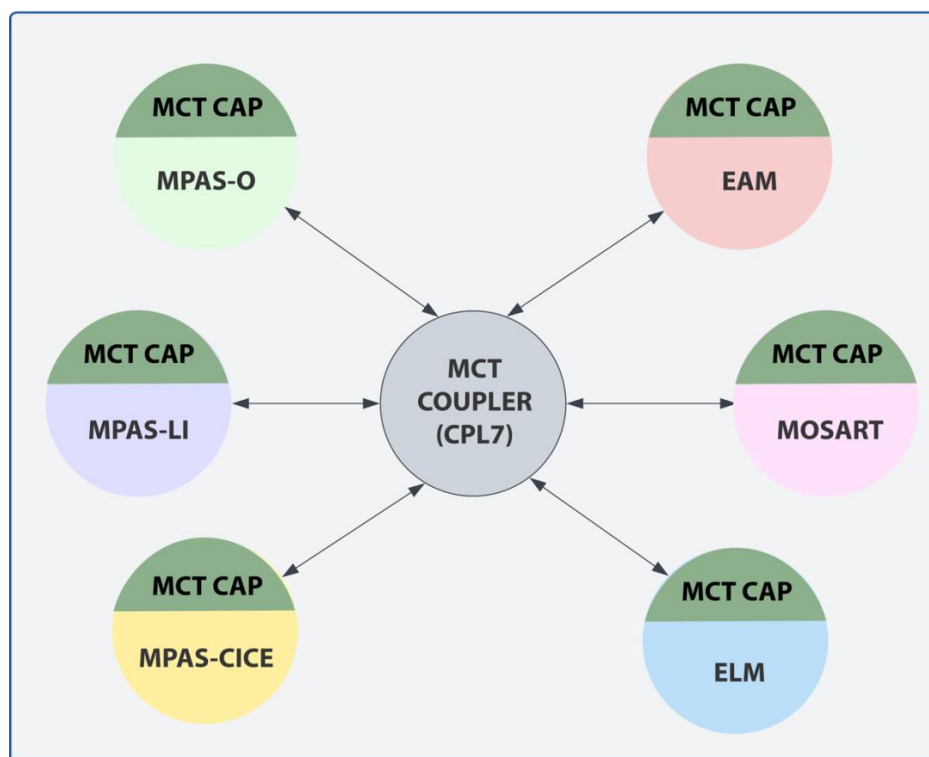
101 simulating surface energy balance and water budget, a process not yet considered by current land models  
102 in WRF (Hao et al., 2021; Yuan et al., 2023).

103 This study integrates ELM v2.1 with WRF (hereafter named WRF-ELM) using a modified coupler  
104 derived from University Corporation for Atmospheric Research (UCAR)'s Lightweight Infrastructure for  
105 Land-Atmosphere Coupling (LILAC) (Ucar, 2020). We evaluate the model performance using a broad  
106 range of site observations and reanalysis data, providing a benchmark for subsequent model enhancements.  
107 This effort expands the capability of a global LSM, which has been previously used within GCM  
108 frameworks, allowing it to simulate higher resolution land-atmosphere interactions at regional scales. The  
109 introduction and release of WRF-ELM also benefit the ELM user community by providing opportunities  
110 for them to test new land schemes with atmospheric feedbacks and calibrate model parameters in coupled  
111 models.

112

## 113 **2. Methods**

### 114 **2.1 Coupler in E3SM**



115

116 **Figure 1** Schematic diagram of the E3SM model components. The top-level coupler (CPL7) serves as the  
117 main program for communication between each component. The Model Coupling Toolkit (MCT) cap in  
118 each component provides an interface between CPL7 and the physical core, which is responsible for  
119 memory allocation, preprocessing, post-processing, and input and output (I/O).

120

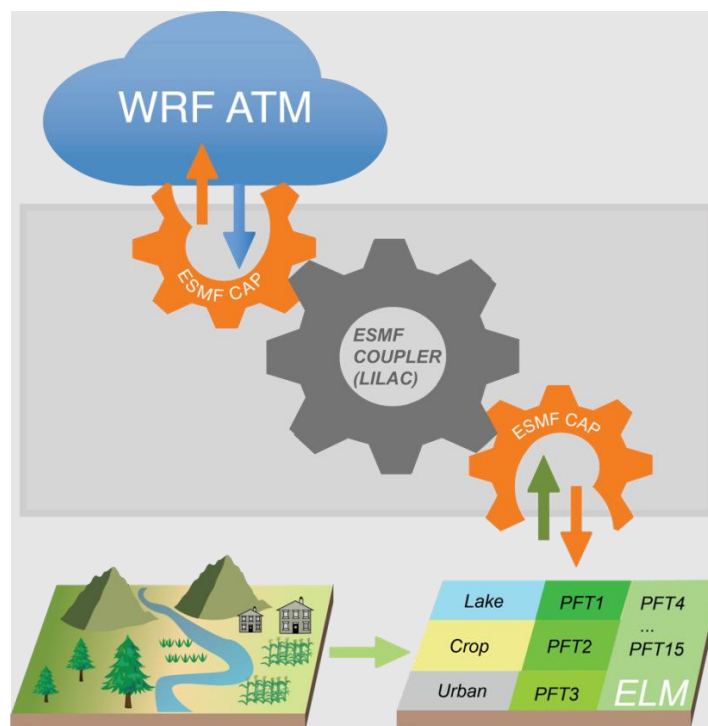
121 E3SM adopts a hub-and-spoke architecture to couple the different model components together, as  
122 shown in Figure 1. In this architecture, communication between the parallel components is realized via the  
123 Model Coupling Toolkit (MCT; (Larson et al., 2005; Jacob et al., 2005)). The top-level coupler, version 7  
124 coupler (CPL7), calls model component initialization, execution, and finalization methods through  
125 specified interfaces (Craig et al., 2012). The MCT cap within each component provides an interface between  
126 the CPL7 and the physical core, which is responsible for memory allocation, preprocessing, post-processing,  
127 and input and output (I/O). Importantly, the inter-component communication is realized only through the



128 central hub, instead of direct communication with one another. The E3SM coupling framework imposes  
129 strict requirements on how an atmospheric model can communicate with ELM. One particular challenge is  
130 that many atmosphere models – including WRF – expect to run the land model in the middle of the time  
131 step sequence. Accomplishing this in the E3SM architecture can require significant restructuring of the  
132 atmosphere model. For this reason, ELM has not been coupled to atmospheric models in the regional model  
133 community, limiting its ability to address complex scientific challenges at fine resolutions.

134

## 135 2.2 LILAC-ESMF Coupler



136

137 **Figure 2** Schematic diagram of the coupling framework for WRF-ELM. The top-level coupler (LILAC) is  
138 in charge of communication between WRF ATM and ELM. The ESMF Cap within ELM and WRF ATM is  
139 responsible for memory allocation, preprocessing, post-processing, and input and output (I/O).

140

141





142           The traditional way of coupling between LSMs (CLM4, Noah, Noah-MP, and SSiB) and WRF is  
143 through internal subroutines and interfaces within the WRF codebase. This tight coupling means that the  
144 LSM is often compiled and run as an integral part of the WRF model. As the LSMs grow to integrate more  
145 land processes, the tight coupling approach can become less scalable and harder to manage. Additionally,  
146 maintaining the coupled system updated with the latest versions of WRF and LSMs can be challenging due  
147 to the need for synchronized updates and compatibility checks. In contrast, modern approaches such as  
148 LILAC-ESMF offer a more modular and flexible way of coupling, facilitating easier integration and updates  
149 of different model components.

150           We have developed an ESMF (Hill et al., 2004) Cap which wraps ELM to facilitate seamless  
151 communication with the central hub driver that connects WRF ATM and ELM (Fig. 2). The central hub  
152 driver, LILAC, is developed using ESMF and provides the fundamental functions to support the integration  
153 of an LSM within an RCM, including 1) creating the list of fields passed from WRF ATM to ELM and vice  
154 versa; 2) initializing ESMF Caps for WRF ATM and for ELM); 3) coordinating calls of the ESMF Caps  
155 and ELM and exchanging data between these components; and 4) providing missing atmospheric fields,  
156 specifically for atmospheric aerosols

157           Within the coupling framework, the ESMF Cap provides the functions of 1) converting the input  
158 data from LILAC to the land model and vice versa; 2) supplying any additional input fields that ELM  
159 requires but are not provided by WRF ATM, for example, gross domestic product, population density, and  
160 lightning that are used to predict fire ignitions in ELM; and 3) setting the domain decomposition and  
161 generating the land mesh. The ESMF cap, which provides the necessary infrastructure to connect LILAC  
162 and ELM physics, serve as an example for similar coupling work between other LSMs and RCMs.

163

### 164 **2.3 Exchange variables between WRF and ELM**

165           ELM is driven by meteorological forcings including precipitation, downward shortwave radiation,  
166 downward longwave radiation, zonal wind at reference height ( $z_{atm}$ ), meridional wind at  $z_{atm}$ , pressure at  
167  $z_{atm}$ , specific humidity at  $z_{atm}$ , and air temperature at  $z_{atm}$ . In the coupled version, the meteorological forcings



168 are provided by WRF ATM with the ELM model timestep set to match the integration timestep in the WRF  
169 ATM. The reference height refers to the height of the lowest atmosphere model level. The radiation scheme  
170 in WRF further splits the shortwave radiation to direct and diffuse components, as well as visible and near-  
171 infrared radiation. Precipitation is divided into rainfall and snowfall based on the frozen precipitation ratio,  
172 which are then inputted into the ELM. The ELM output includes skin temperature, 2-m air temperature, 2-  
173 m specific humidity at the surface, friction velocity, surface albedo, sensible heat flux, latent heat flux,  
174 ground heat flux, surface emissivity, and roughness length for momentum and heat transfer, which will be  
175 exchanged with the WRF ATM component.

176

#### 177 **2.4 Mesh data and surface parameters**

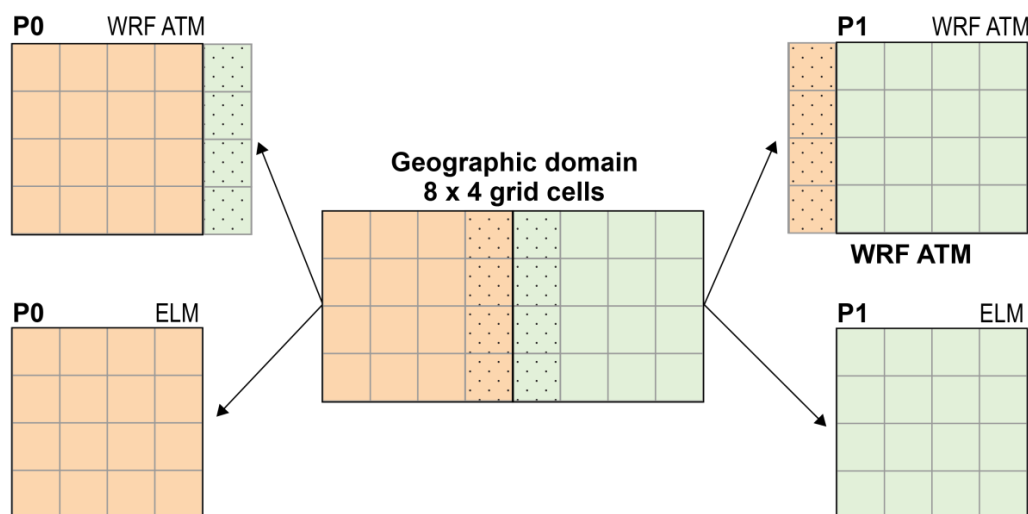
178 In addition, mesh data is used in the WRF ATM to define the latitude and longitude of the grid. The  
179 domain information is necessary for the coupler and the land model during runtime. These data include a  
180 mask that informs the land model where to run and a land fraction that the coupler uses to combine fluxes  
181 from various surface types over a grid cell. The surface data configures the spatially implicit features (e.g.,  
182 spatial fraction coverage, leaf and soil albedo, leaf and soil emissivity, etc.) of subgrid elements within grid  
183 cells (topographic unit, land cover, soil columns, and vegetation).

184 While a regular latitude/longitude grid is widely used for domain and surface data in the land-only  
185 mode, when coupled with WRF ATM, ELM needs to adopt the Lambert Conformal projection used in WRF.  
186 To create a domain file of Lambert Conformal projection, a grid descriptor file based on the WRF Pre-  
187 Processing System (WPS) output (e.g., geo\_em.d01) needs to be created, which is then used to create the  
188 domain file used in ELM. A similar workflow is needed for surface data, which contains a large number of  
189 input files that need to be interpolated by the land model. To generate both domain files and surface data, we  
190 employ the ELM preprocessing tools that derive the input data and grid descriptor files for each dataset,  
191 produce mapping files from the input data grid to our target grid, and then use the mapping weight files for  
192 interpolation.

193



194 **2.5 Parallelization**



195

196 **Figure 3** Schematic of parallel domain decomposition scheme in WRF-ELM. The dotted area indicates  
197 ‘halo’ arrays in which memory is shared between processors (P0 and P1). WRF ATM and ELM are  
198 calculated under the same processor.

199

200 Instead of adopting ELM’s native round-robin domain decomposition strategy, our parallelization  
201 strategy for WRF-ELM is to use geographic domain decomposition, as in WRF ATM. As shown in Fig. 3,  
202 different grid cells in the model’s physical domain are running on separate processors pre-assigned by the  
203 user. On each processor, ELM within WRF employs parallel I/O to read atmospheric forcings, uses the  
204 surface properties and land-use datasets to configure individual land cells, and then conducts massively  
205 parallel simulations over these grid cells within each subdomain independently. In WRF ATM, the ‘halo’  
206 arrays share memory between processors, and message passing between processors is accomplished using  
207 the message passing interface (MPI; (Gropp et al., 1996)).

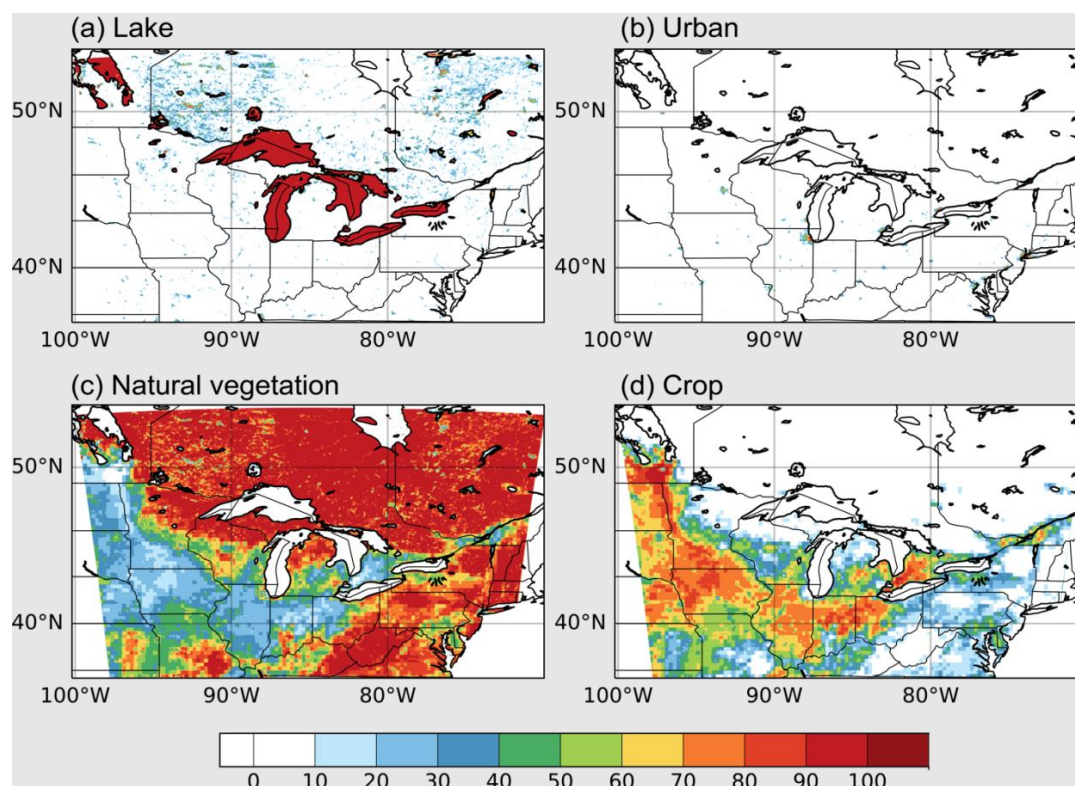
208

209 **3. Model Validation**



210 **3.1 WRF-ELM configuration**

211 For our first WRF-ELM application, we study the land-atmosphere interactions over the Great  
212 Lakes Region (GLR), a hydrodynamically complex and heavily populated region with both natural surface  
213 heterogeneity and significant land management practices. This domain also includes the world's largest  
214 freshwater system, comprising of Superior, Michigan, Huron, Erie, and Ontario Lakes. This region is the  
215 focus of the U.S. Department of Energy's (DOE's) Coastal Observations, Mechanisms, and Predictions  
216 Across Systems and Scales, Great Lakes Modeling (COMPASS-GLM) project, which has an overall goal  
217 of developing a fully coupled (lake-land-atmosphere) regional earth system model centered on the GLR  
218 (Kayastha et al., 2023). Here, we report the initial implementation of the WRF-ELM framework to support  
219 its ability to capture atmospheric, coastal, urban, and rural interactions, providing a baseline reference  
220 solution for further model development.



221



222 **Figure 4** Fractional coverage (%) of major land unit (a) lake, (b) urban, (c) natural vegetation, and (d) crop  
 223 used in the WRF-ELM.

224

225 The RCM used in the numerical simulation is based on the WRF model version 4.4.2 with the  
 226 Advanced Research WRF dynamic core (Skamarock and Klemp, 2008). Following Wang et al. (2022a), the  
 227 model domain is centered at 45.5°N and 85.0°W and has dimensions of 544 × 485 grid points in the west–  
 228 east and south–north directions. The simulation domain covers the GLR, with a spatial resolution of 4 km  
 229 (Fig. 4). Fifty vertical layers from the surface to 50 hPa are adopted with denser layers at lower altitudes to  
 230 sufficiently resolve the PBL. We conduct 5 ensemble members in 2018, starting with initial conditions 12  
 231 hr apart between 0000 UTC on 12 May and 0000 UTC on 14 May and ending on 0000 UTC 1 September  
 232 2018. The resulting simulations are analyzed during June, July, and August (JJA) 2018.

233

**Table 1** Model Configuration in WRF and ELM.

WRF specific options and schemes	
Meteorological IC/LBCs	ERA5
Microphysics	Thompson microphysics
Radiation	RRTMG for longwave and shortwave
Land surface	ELM or CTSM
Planetary boundary layer	YSU scheme
Lake surface temperature	NOAA GLSEA
ELM/CTSM input data	
Land use and land cover	ELM/CTSM default parameter
Vegetation	ELM/CTSM default parameter
Soil color	ELM/CTSM default parameter
topography	ELM/CTSM default parameter
Number of plant functional types (PFT)	16

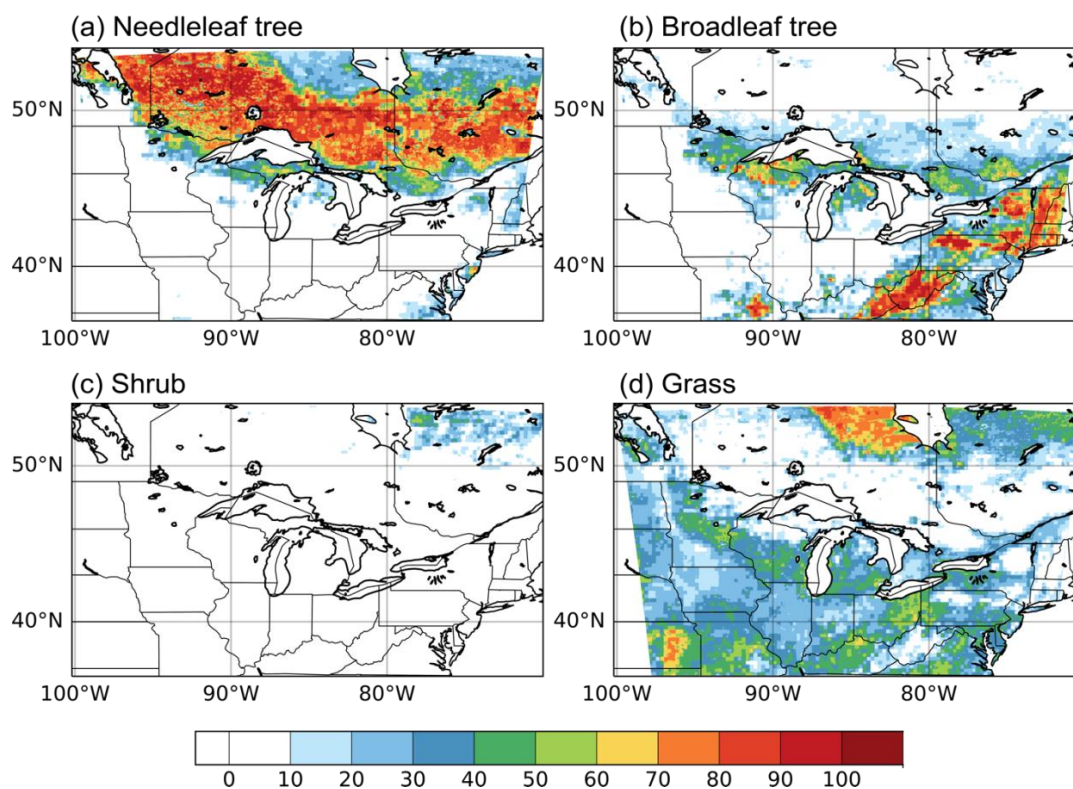
234

235 The meteorological initial condition (IC) and lateral boundary conditions (LBCs) have been derived  
 236 from the ECMWF Reanalysis v5 (ERA5; (Hersbach et al., 2020)) at 0.25° horizontal resolution and 3-hour  
 237 temporal intervals (Table 1). The WRF model incorporates the Thompson microphysics (Thompson et al.,  
 238 2004; Thompson et al., 2008), the Rapid Radiative Transfer Model for GCMs longwave and shortwave  
 239 schemes (Iacono et al., 2008), and the Yonsei University planetary boundary layer scheme (Hong and Lim,



240 2006). We turn off cumulus parameterization, considering the convection-permitting resolution of the  
241 ensemble simulations. The lake skin temperature is obtained from NOAA Great Lakes Surface  
242 Environmental Analysis (GLSEA) data set (Schwab et al., 1992) derived from Advanced Very High-  
243 Resolution Radiometer.

244 For the land surface model, we adopt ELM with satellite phenology (ELM-SP) mode which utilizes  
245 seasonal varying leaf area index prescribed based on the MODIS data. The default ELM land surface  
246 parameters have been used in the coupled model simulation, including land use and land cover information,  
247 vegetation biogeophysical properties, soil properties, and topography. The surface parameter is also  
248 applicable in CTSM (Table 1). A detailed description of ELM/CTSM default parameter can be found in (Li  
249 et al., 2024). The current version of WRF-ELM does not enable biogeochemistry (ELM-BGC) mode and  
250 thus does not simulate carbon and nitrogen cycles. In addition, we also conduct simulations using the WRF  
251 coupled with Community Terrestrial Systems Model (CTSM ctsm5.1.dev114) (Lawrence et al., 2019)  
252 (WRF-CTSM hereafter), which can be used to compared with WRF-ELM's performance in capturing the  
253 land-atmosphere exchanges of energy and water fluxes. CTSM is also referred to the community land model  
254 version 5 (CLM5) afterwards.



255

256 **Figure 5** Fractional coverage (%) of major plant functional types (a) needleleaf forest (deciduous and  
257 evergreen combined), (b) broadleaf forest (deciduous and evergreen combined), (c) shrub, and (d) grass  
258 used in the WRF-ELM.

259

260 It is noteworthy that there are several distinctions between WRF-ELM and the version of WRF-  
261 CTSM we use here. WRF-CTSM aims for a relatively fast calculation speed, thus it has simplified the  
262 description of land cover and kept the single dominant land unit and single dominant PFT. In our simulation  
263 region, WRF-CTSM identifies the Great Lakes in the center of the simulation domain, with the natural  
264 vegetation prevailing in the northern and southeastern regions, and crops dominating the southwestern areas  
265 (Fig. 4). On the other hand, WRF-ELM preserves the comprehensive description of subgrid heterogeneity.  
266 As a result, the fluxes calculated from various surface types are merged using a weighted-average method  
267 before transferring to the upper-level WRF ATM. This is particularly important in regions with mixed





268 vegetation types, such as the southwestern part of our study domain. Moreover, within the natural  
 269 vegetation land unit, WRF-ELM simulates the blend of needleleaf and broadleaf trees (evergreen and  
 270 deciduous combined) around the Great Lakes and the mixture of crops and grasses in the southwestern part  
 271 of the domain (Fig. 5).

272

### 273 3.2 Data for validation

274 **Table 2** Dataset for validation in the study.

Dataset	Variables	Spatial resolution	Temporal resolution	Reference
ASOS	Air temperature at 2-m, Dew point	point	Hourly	(Nadolski, 1992)
AmeriFlux	Latent heat, Sensible heat	point	Hourly	(Law, 2005)
Daymet	Maximum air temperature at 2-m, Maximum air temperature at 2-m, Precipitation	1 km	Monthly	(Thornton et al., 2022)
NLDAS	Air temperature at 2-m, Precipitation	0.125 °	Monthly	(Xia et al., 2012)
ERA5-Land	Air temperature at 2-m, Precipitation, Latent heat, Sensible heat	9 km	Monthly	(Muñoz-Sabater et al., 2021)

275

276 Observational and reanalysis data from multiple sources have been used to evaluate WRF  
 277 simulation results (Table 2). We select 12 paired sites from the Automated Surface Observing System  
 278 (ASOS) to acquire 5-minute 2-meter air temperature ( $T_a$ ) and 2-meter dew point temperature over the urban  
 279 and rural area in the GLR (<https://www.ncei.noaa.gov>; last accessed: November 2023). The 2-meter relative  
 280 humidity (RH) is derived from  $T_a$  and dew point. We compute hourly averages of  $T_a$  and RH from the 5-  
 281 minute data to match the hourly WRF outputs.

282





283 **Table 3** AmeriFlux site information (LCF: land cover type; DBF: deciduous broadleaf tree; MF: mixed  
 284 forest; NEON: National Ecological Observatory Network)

Site ID	Latitude	Longitude	LCF	PI(s)	DOI
US-xST	45.5089	-89.5864	DBF	NEON	<a href="https://doi.org/10.17190/AMF/1617737">https://doi.org/10.17190/AMF/1617737</a>
US-xTR	45.4937	-89.5857	DBF	NEON	<a href="https://doi.org/10.17190/AMF/1634886">https://doi.org/10.17190/AMF/1634886</a>
US-WCr	45.8059	-90.0799	DBF	Ankur Desai	<a href="https://doi.org/10.17190/AMF/1246111">https://doi.org/10.17190/AMF/1246111</a>
US-xUN	46.2339	-89.5373	MF	NEON	<a href="https://doi.org/10.17190/AMF/1617741">https://doi.org/10.17190/AMF/1617741</a>
US-PFa	45.9459	-90.2723	MF	Ankur Desai	<a href="https://doi.org/10.17190/AMF/1246090">https://doi.org/10.17190/AMF/1246090</a>
US-Syv	46.242	-89.3477	MF	Ankur Desai	<a href="https://doi.org/10.17190/AMF/1246106">https://doi.org/10.17190/AMF/1246106</a>

285

286 In addition, we collect measurements of latent heat (LH) and sensible heat (SH) from six flux tower  
 287 sites provided by AmeriFlux (<http://ameriflux.lbl.gov>; last accessed: November 2023). Initially, 16  
 288 AmeriFlux sites have been selected within our study domain for the JJA 2018 period, which included  
 289 measurements over grassland, mixed forest, and deciduous broadleaf forest. However, ten sites are filtered  
 290 out because their land cover types differ from the dominant ones used in WRF-CTSM. The latitudes and  
 291 longitudes of selected sites have been documented in Table 3. The hourly LH and SH data from AmeriFlux  
 292 have been reduced to daily averages to validate the model simulation of surface energy fluxes.

293 We also acquire reanalysis datasets to evaluate the model performance in simulating the climate  
 294 variables and energy fluxes. All datasets are resampled using bilinear interpolation to a 4 km resolution to  
 295 align with the WRF grids. We employ the Daymet dataset from <https://daymet.ornl.gov> (last accessed:  
 296 October 2023), which provides daily, gridded (1 km × 1 km) estimates of solar radiation, 2-meter maximum  
 297 (Tmax) and minimum (Tmin) temperature, precipitation (PRE), snow water equivalent, and water vapor  
 298 across the CONUS (Thornton et al., 2022). It uses local regression algorithms to interpolate and extrapolate  
 299 daily meteorological observations from Global Historical Climatology Network (GHCN). Daymet  
 300 considers the effects of elevation on climate and generates daily meteorological variables for a particular  
 301 grid cell using the weighted linear regression-based approach. We download monthly Tmax, Tmin, and



302 precipitation from Daymet version 4.5, and average the temperatures to compare against model simulated  
303 daily mean  $T_a$ .

304 Monthly  $T_a$  from the North American Land Data Assimilation System version 2 (NLDAS) with  
305 Noah LSM is used as an additional source of reanalysis data to evaluate WRF-ELM. These data are  
306 available beginning in 1979 at a  $0.125^\circ$  resolution (Xia et al., 2012). NLDAS constructed a forcing dataset  
307 from a daily gauge-based precipitation analysis, bias-corrected shortwave radiation, and surface  
308 meteorology reanalyses from North American Regional Reanalysis (NARR) to drive four different LSMs  
309 to derive surface fluxes and state variables. We acquire the product derived using the Noah model  
310 (<https://disc.gsfc.nasa.gov>; last accessed: October 2023) because it is one of the most commonly used LSMs  
311 and has been frequently coupled with climate and atmospheric models.

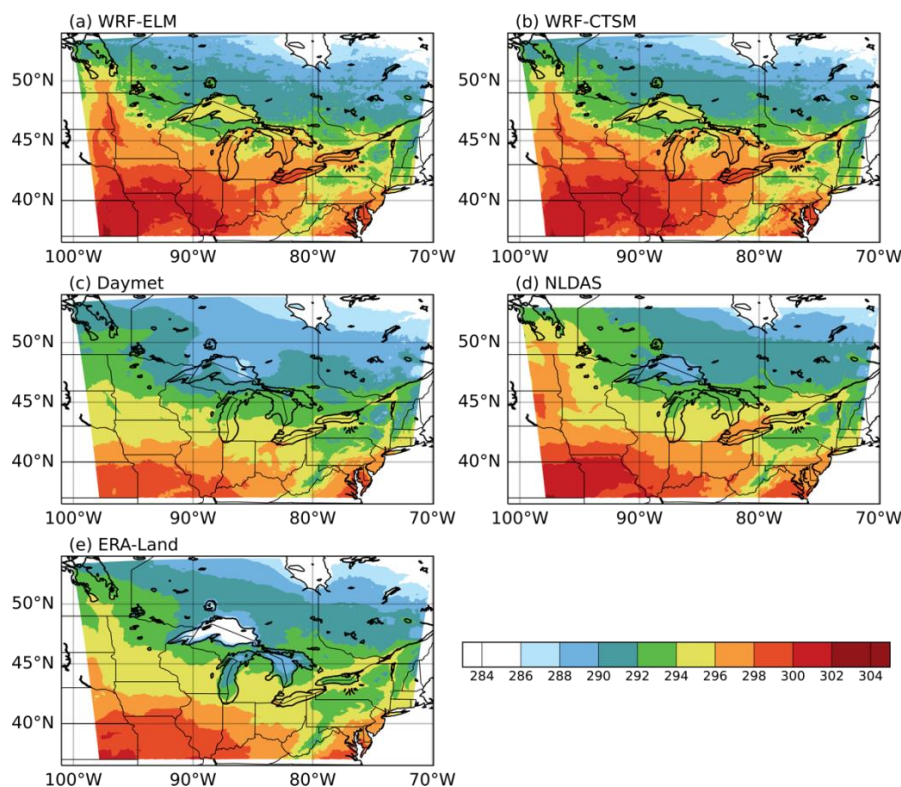
312 The ERA5-Land reanalysis provides surface variables at the  $0.1^\circ \times 0.1^\circ$  resolution (Muñoz-Sabater,  
313 2019). The data are produced under the offline mode forced by meteorological fields from ERA5 (Muñoz-  
314 Sabater et al., 2021), without coupling to the atmospheric module of the ECMWF's Integrated Forecasting  
315 System. ERA5-Land datasets have also been widely used for a variety of land condition assessments (Pelosi  
316 et al., 2020; Stefanidis et al., 2021; Wang et al., 2022b). We acquire monthly  $T_a$ , SH, and LH in ERA5-  
317 Land from Google Earth Engine (collection ECMWF/ERA5\_LAND/MONTHLY\_AGGR; last accessed:  
318 October 2023).

319 Lastly, we acquire precipitation data from the National Centers for Environmental Prediction  
320 (NCEP) Stage IV dataset (Lin and Mitchell, 2005), a gridded product with 4 km spatial and hourly temporal  
321 resolution that covers the period from 2002 to the present. NCEP compiles the Stage IV product using data  
322 from 140 radars and approximately 5,500 gauges across the CONUS. Stage IV provides highly accurate  
323 precipitation estimates, particularly for medium to heavy precipitation, and has therefore been widely used  
324 as a reference for precipitation evaluation (Nelson et al., 2016).

325

### 326 **3.3 Results**

#### 327 **3.3.1 Temperature**



328

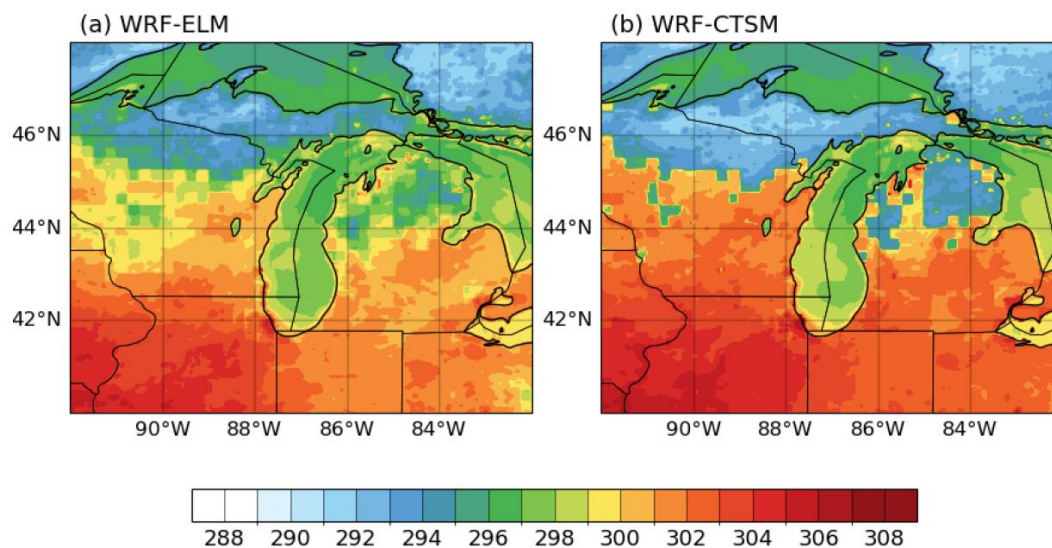
329 **Figure 6** June-July-August mean 2-m air temperature (K) in (a) WRF-ELM, (b) WRF-CTSM, (c) Daymet,  
 330 (d) NLDAS, and (e) ERA-Land. The numbers on the top right of (c)-(f) indicate the spatial correlation  
 331 coefficient between each reanalysis product and the two simulation results.

332

333 **Table 4** Evaluation metrics of June-July-August 2-m air temperature between each model result and the  
 334 reanalysis product. CORR: spatial correlation coefficient; RMSE: Root mean square error.

		Daymet	NLDAS	ERA-Land
WRF-ELM	Bias	1.70	0.34	1.20
	CORR	0.94	0.94	0.86
	RMSE	2.18	1.43	2.30
WRF-CTSM	Bias	1.79	0.43	1.29
	CORR	0.94	0.93	0.86
	RMSE	2.30	1.57	2.40

335



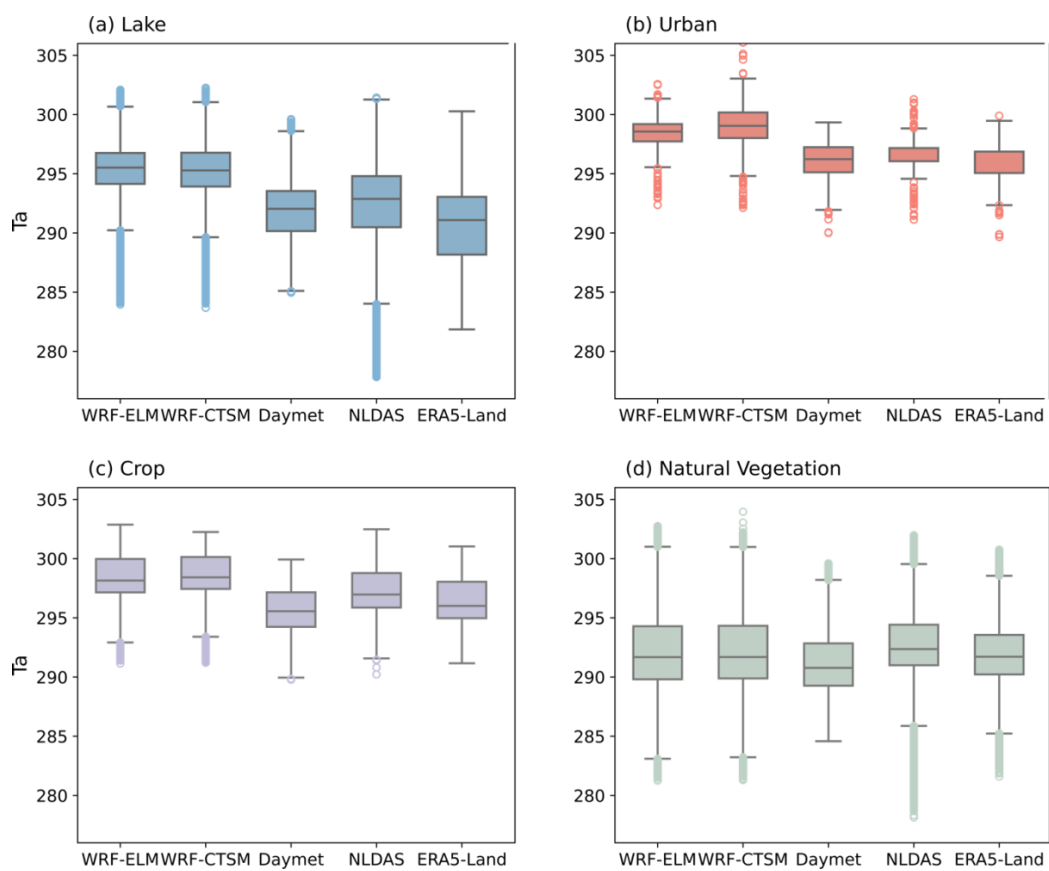
336

337 **Figure 7** June-July-August mean skin temperature (K) in (a) WRF-ELM, (b) WRF-CTSM, zoomed-in view

338 focuses on the area surrounding Lake Michigan

339

340 The spatial distribution of  $T_a$  from the WRF-ELM and WRF-CTSM models, along with reanalysis  
341 data such as Daymet, NLDAS, and ERA5-Land, is illustrated in Figure 6. Both WRF-ELM and WRF-  
342 CTSM have reasonably captured the spatial pattern observed in the reanalysis datasets, demonstrating a  
343 spatial correlation coefficient (CORR) ranging from 0.86 to 0.95 (Table 4). The highest CORR is observed  
344 with Daymet, while the lowest one is with ERA5-Land. Both models exhibit a warm bias compared to  
345 reanalysis products. However, WRF-ELM shows a slightly lower bias and RMSE compared with WRF-  
346 CTSM (Table 4). Additionally, WRF-ELM displays a smoother gradient in comparison to WRF-CTSM,  
347 particularly over the GLR where needleleaf trees, broadleaf trees, grasses, and croplands coexist (Fig. 7).



348

349 **Figure 8** Boxplots of June-July-August 2-m air temperature (K) over (a) lake, (b) urban, (c) crop, and (d)

350 natural vegetation in simulations and reanalysis products.

351

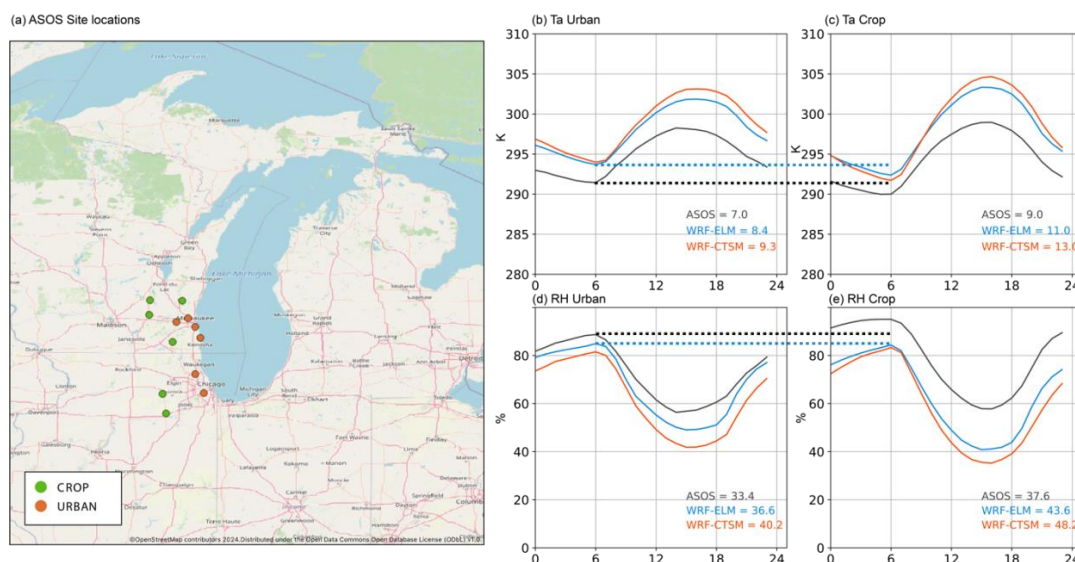
352 **Table 5** June-July-August 2-m air temperature over each land unit in simulations and reanalyses.

	WRF-ELM	WRF-CTSM	Daymet	NLDAS	ERA5-Land
Lake	295.5	295.4	292.1	292.3	290.6
Urban	298.5	299.0	296.2	296.7	296.0
Crop	298.4	298.6	295.8	297.4	296.5
Natural Vegetation	292.6	292.6	291.7	292.9	292.4



353

354 Despite the overall good performance of model simulation of Ta, it is slightly different among  
 355 different land units (Fig. 8). The largest warm bias is found over the lake surface, in which both models  
 356 have overestimated Ta by 3-5 K (Table 5, Fig. 8). For urban and crop areas, the WRF-ELM and WRF-  
 357 CTSM show a slightly warmer temperature by 2-3 K than all reanalysis data, which makes sense since  
 358 reanalysis datasets do not capture urban-scale warming signals (Chen et al., 2024). The Ta over the natural  
 359 vegetation is well captured, with the average value in both models within the range of average Ta over all  
 360 datasets.



361

362 **Figure 9** (a) The location of ASOS sites. (b-c) June-July-August averaged hourly 2-meter air temperature  
 363 over (b) urban and (c) crop land units for ASOS, WRF-ELM, and WRF-CTSM. (d-e) The same as (b-c) but  
 364 for 2-meter relative humidity. The numbers in (b-e) indicate the diurnal ranges of air temperature and  
 365 relative humidity from ASOS, WRF-ELM, and WRF-CTSM. The dash lines highlight the nighttime Ta and  
 366 RH when urban and crop contrasts are significant.

367

368 We use ASOS sites to examine the representation of urban heat island (UHI; (Rizwan et al., 2008))  
 369 and urban dry island (UDI; (Chakraborty et al., 2022b)) effects in WRF-ELM and WRF-CTSM. Six urban



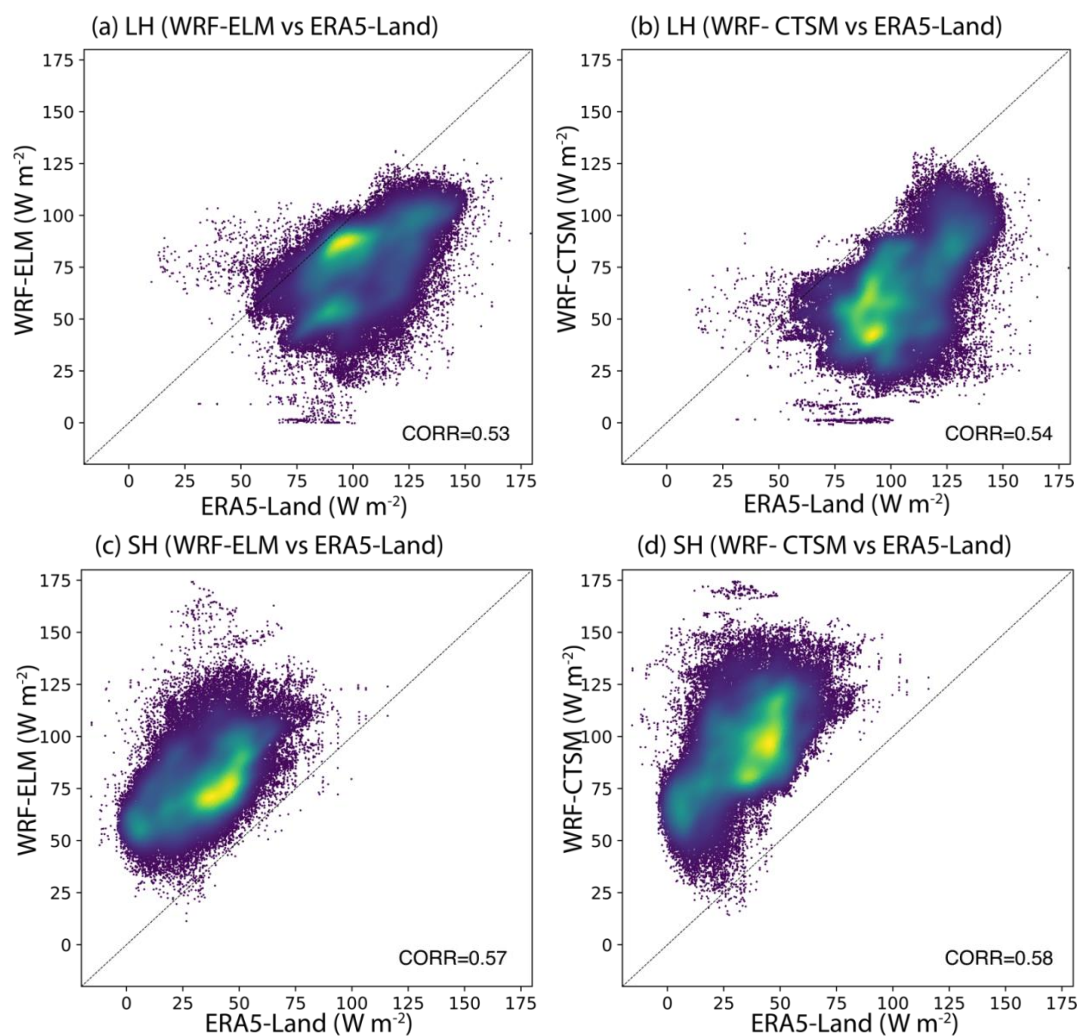
370 sites on the west coast of Lake Michigan have been selected, and correspondingly, six crop sites near the  
371 urban sites are chosen as pair sites (Fig. 9a). Compared to the adjacent rural sites, the urban sites exhibit a  
372 higher minimum  $T_a$  during the night and early morning, leading to a reduced diurnal temperature range of  
373 7.0 K, compared to the 9.0 K range over the crop sites (Figs. 9b-c). During the late morning to noon, the  
374 lake breeze tends to cool the urban air temperature, resulting in lower daily maximum  $T_a$  than over the crop  
375 areas (Wang et al., 2023). In the afternoon, the urban sites display a more gradual temperature change slope  
376 than the rural sites, attributable to the cumulative heating effect of solar radiation absorption and heat release  
377 by urban materials throughout the day (Soltani and Sharifi, 2017). The UDI effect is also discernible in the  
378 2m RH in ASOS observations, with urban areas exhibiting lower values at night (Figs. 9d-e). Both WRF-  
379 ELM and WRF-CTSM have captured the warmer  $T_a$  and lower RH during the night and the smaller diurnal  
380 range of  $T_a$  and RH in urban compared with crop sites. Notably, WRF-ELM generally demonstrates smaller  
381 biases in both  $T_a$  and RH than WRF-CTSM (Figs. 9).

382

### 383 **3.3.2 Energy fluxes**

384

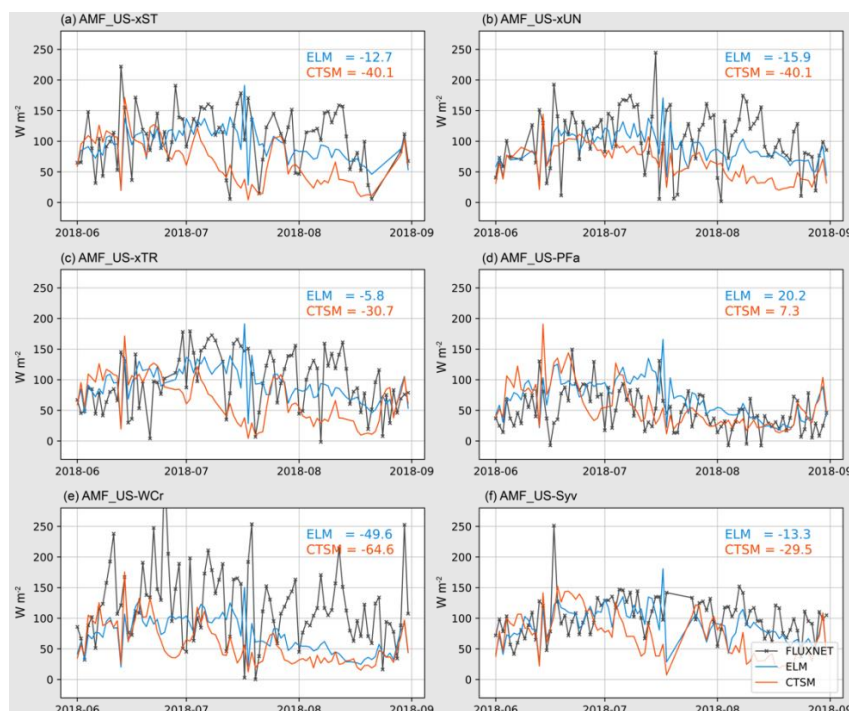




385

386 **Figure 10** Comparison of latent heat over natural vegetation land unit between (a) WRF-ELM and ERA5-  
387 Land and (b) WRF-CTSM and ERA5-Land. (c)-(d) Same as (a)-(b) but for sensible heat. Each point  
388 represents the JJA mean surface fluxes in a grid.





389

390 **Figure 11** June-July-August averaged daily LH fluxes from six AmeriFlux sites and the corresponding  
 391 model grids. The numbers indicate biases between WRF-ELM (or WRF-CTSM) and AmeriFlux.

392

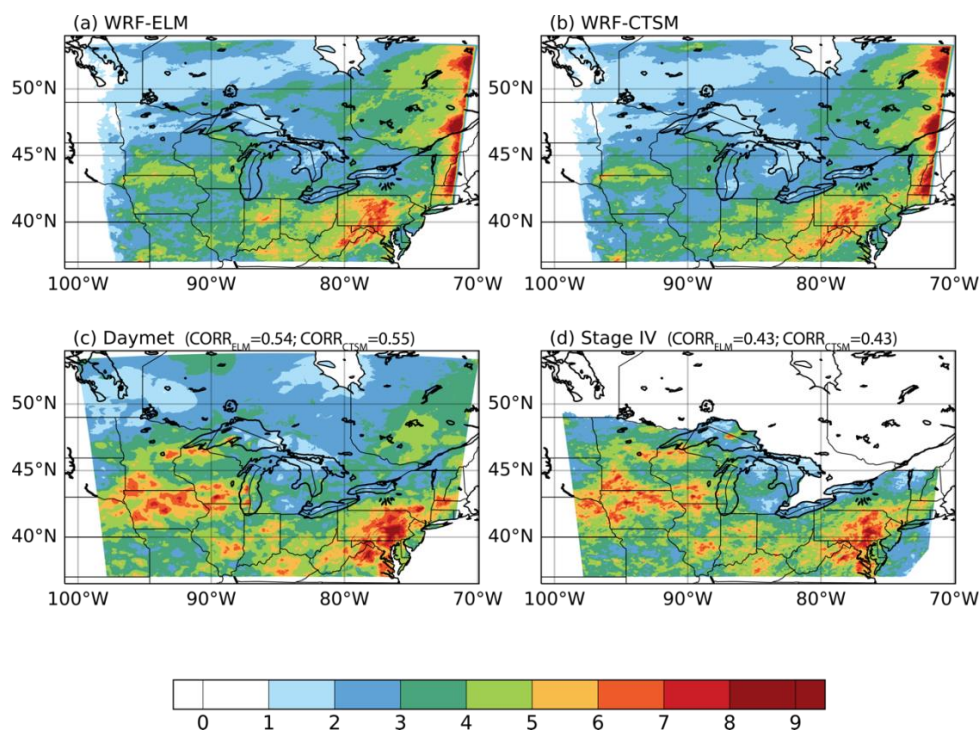
393 We evaluate the simulated LH and SH fluxes from model simulations against ERA5-Land. The  
 394 spatial CORR ranging from 0.53 to 0.58 (Fig. 10). An underestimation of LH and an overestimation of SH  
 395 are evident for both WRF-ELM and WRF-CTSM compared to ERA5-Land. A further comparison of daily  
 396 LH values from six AmeriFlux sites over deciduous broadleaf forest is illustrated in Figure 11. The observed  
 397 temporal variations of LH, largely influenced by incoming solar radiation and precipitation, are roughly  
 398 captured in both WRF-ELM and WRF-CTSM. Compared to the daily observations from AmeriFlux sites,  
 399 WRF-ELM demonstrates a superior ability to reproduce the observed magnitude of LH and exhibits a  
 400 smaller bias than WRF-CTSM (Fig. 11)

401

### 402 3.3.3 Precipitation



403



404

405 **Figure 12** The spatial distribution of June-July-August precipitation (mm d<sup>-1</sup>) in (a) WRF-ELM, (b) WRF-  
406 CTSM, (c) Daymet, and (d) ST4. The numbers on the top right of (c)-(d) indicate the CORR between each  
407 observational product and the two simulation results.

408

409 Figure 12 presents the spatial distribution of precipitation from models and observations. It is  
410 important to note that Stage IV primarily focuses on the CONUS region, while significant areas of our  
411 simulation domain in Canada remain uncovered. Compared with the Daymet ( $PRE_{\text{Daymet}} = 3.55 \text{ mm d}^{-1}$ ),  
412 both WRF-ELM and WRF-CTSM capture the regional mean value ( $PRE_{\text{WRF-ELM}} = 3.14 \text{ mm d}^{-1}$  and  $PRE_{\text{WRF-CTSM}} = 2.96 \text{ mm d}^{-1}$ ) and the spatial distribution of precipitation, exhibiting CORR ranging from 0.43 to 0.55.  
413  
414 The precipitation over the southeastern part of our study domain is well captured while that on the western  
415 side of Lake Michigan is slightly underestimated, with WRF-ELM demonstrating a lower bias than WRF-  
416 CTSM. This underestimation of precipitation aligns with the underestimation of latent heat and



417 evapotranspiration, suggesting that suppressed evapotranspiration may reduce moisture availability and  
418 transport, particularly to the western GLR. Conversely, an overestimation of precipitation is evident along  
419 the eastern boundary of our study domain.

420

#### 421 **4. Discussion and Conclusions**

422 This study introduces a framework integrating the state-of-the-art land surface model, ELM, with  
423 the widely used regional weather and climate model, WRF, named WRF-ELM. Moving beyond the  
424 traditional way of coupling between LSMs and WRF through internal subroutines within the WRF codebase.  
425 We adopt the LILAC-ESMF framework, a modular approach which maintains the integrity of the ELM's  
426 source code structure and facilitates the transfer of future developments in ELM to WRF-ELM. After  
427 coupling the two models, simulations using WRF-ELM have been conducted over the Great Lakes Region,  
428 and their performance has been evaluated against observations and reanalysis data from multiple sources  
429 and the WRF-CTSM simulations. These model simulations have been conducted at a resolution of  $4 \text{ km} \times$   
430  $4 \text{ km}$ , facilitating direct model validation and verification with various data sources. The use of seasonal  
431 mean simulation outputs and diurnal cycles showcases the capabilities of WRF-ELM in representing the  
432 temporal and spatial variations of water and energy cycles over the Great Lakes Region.

433 In general, our findings suggest that the newly coupled WRF-ELM effectively captures the spatial  
434 distribution of surface state variables and fluxes across the GLR. The model displays a smoother gradient  
435 in surface skin temperature than WRF-CTSM, due to the representation of sub-grid features within grid  
436 cells. The model's performance is particularly reasonable over the natural vegetation, while a minor warm  
437 bias is detected over crop and urban grids.

438 The slight overestimation of air temperature in crop regions could potentially be mitigated by  
439 incorporating a more realistic representation of crops, such as crop rotation and irrigation. Additionally, the  
440 application of spatially varying crop parameters closely captures the observed magnitude and seasonality  
441 of carbon and energy fluxes compared to the observations (Sinha et al., 2023). However, these  
442 improvements have only been tested using the land-only ELM. Our generalized coupling framework



443 supports future studies of sophisticated crop-atmosphere interactions at finer spatial resolution than those  
444 achieved with coarse GCM simulations.

445 In addition, the UHI effects in cities surrounding the GLR are generally captured in both WRF-  
446 ELM and WRF-CTSM, as indicated by the warmer night temperature in the cities. While there is an  
447 overestimation of UHI compared to ASOS, this could be due to the simplified urban representation in ELM.  
448 For instance, the urban surface emissivity in CLM, and thus ELM due to the shared model structure, is  
449 reported to be noticeably lower than the values derived from satellites, resulting in a surface UHI effect that  
450 is significantly higher than satellite-derived values (Chakraborty et al., 2021). Another potential  
451 contributing factor could be the lack of representation of urban vegetation. The presence of vegetation tends  
452 to mitigate the UHI effect (Paschalis et al., 2021) , and its absence in the urban subgrid would lead to an  
453 overestimation of UHI values, all else remaining equal.

454 Our research develops the WRF-ELM framework and provides the first assessment of its  
455 capabilities through high-resolution model simulations that fully capture expected patterns of land-  
456 atmosphere interactions. Based on the validation and assessment of WRF-ELM results, this study delivers  
457 a baseline reference, identifies common model biases in high-resolution regional applications, and proposes  
458 pathways for subsequent model development for ELM, as well as the coupled model. The coupled model  
459 provides an opportunity to investigate the impact of more sophisticated land processes, such as plant  
460 hydraulics, dynamic vegetation distributions, and soil biogeochemistry, on weather and climate predictions.

461

462 **Author contributions:** HH designed the study, implemented the parameterization, performed the  
463 simulations, analyzed the results, and drafted the original paper. YQ designed the study, discussed the results,  
464 and edited the paper. GB, TT, BS, YL, and WS helped with the coupling design. JW, TT, DH, JL, ZY, PX,  
465 EC and RH discussed the results and edited the paper.

466

467 **Code Availability:** The description and codes of E3SM v2.1 (including ELM v2.1) are publicly available  
468 at <https://doi.org/10.11578/E3SM/dc.20230110.5> and [28](https://github.com/E3SM-</a></p></div><div data-bbox=)



469 Project/E3SM/releases/tag/v2.1.0 (last access: 12 May 2023), respectively. Starting from ELM 2.1, the  
470 model codes for WRF-ELM coupling described in this paper are available at  
471 <https://github.com/hhllbao93/ELM> and <https://doi.org/10.5281/zenodo.11289807> (Huang, 2024).

472

473 **Competing interests:** The authors declare that they have no conflict of interest.

474

475 **Acknowledgement:** The authors acknowledge the CTSM developer teams for making the LILAC release  
476 available including Mariana Vertenstein, Negin Sobhani, Samuel Levis, David Lawrence, Michael Barlage,  
477 Joe Hammann, and Erik Kluzek.

478

479 **Financial support:** This study is supported by COMPASS-GLM, a multi-institutional project supported  
480 by the U.S. Department of Energy (DOE), Office of Science, Office of Biological and Environmental  
481 Research, Earth and Environmental Systems Modeling program. T.C.'s contribution was also supported by  
482 the DOE, Office of Science, Biological and Environmental Research program through an Early Career  
483 award. The Pacific Northwest National Laboratory is operated for DOE by Battelle Memorial Institute  
484 under contract DE-AC05-76RL01830.

485

486



487

488 Reference:

- 489 Ban-Weiss, G. A., Bala, G., Cao, L., Pongratz, J., and Caldeira, K.: Climate forcing and response to  
490 idealized changes in surface latent and sensible heat, *Environ Res Lett*, 6, 034032, 2011.
- 491 Best, M. J., Abramowitz, G., Johnson, H. R., Pitman, A. J., Balsamo, G., Boone, A., Cuntz, M., Decharme,  
492 B., Dirmeyer, P. A., Dong, J., Ek, M., Guo, Z., Haverd, V., van den Hurk, B. J. J., Nearing, G. S., Pak, B.,  
493 Peters-Lidard, C., Santanello, J. A., Stevens, L., and Vuichard, N.: The Plumbing of Land Surface Models:  
494 Benchmarking Model Performance, *J Hydrometeorol*, 16, 1425-1442, [https://doi.org/10.1175/JHM-D-14-](https://doi.org/10.1175/JHM-D-14-0158.1)  
495 0158.1, 2015.
- 496 Binsted, M., Iyer, G., Patel, P., Graham, N. T., Ou, Y., Khan, Z., Kholod, N., Narayan, K., Hejazi, M., Kim,  
497 S., Calvin, K., and Wise, M.: GCAM-USA v5.3\_water\_dispatch: integrated modeling of subnational US  
498 energy, water, and land systems within a global framework, *Geosci. Model Dev.*, 15, 2533-2559,  
499 10.5194/gmd-15-2533-2022, 2022.
- 500 Bisht, G., Huang, M., Zhou, T., Chen, X., Dai, H., Hammond, G. E., Riley, W. J., Downs, J. L., Liu, Y., and  
501 Zachara, J. M.: Coupling a three-dimensional subsurface flow and transport model with a land surface  
502 model to simulate stream-aquifer-land interactions (CP v1.0), *Geosci. Model Dev.*, 10, 4539-4562,  
503 10.5194/gmd-10-4539-2017, 2017.
- 504 Burrows, S., Maltrud, M., Yang, X., Zhu, Q., Jeffery, N., Shi, X., Ricciuto, D., Wang, S., Bisht, G., and  
505 Tang, J.: The DOE E3SM v1. 1 biogeochemistry configuration: Description and simulated ecosystem-  
506 climate responses to historical changes in forcing, *J Adv Model Earth Sy*, 12, e2019MS001766, 2020.
- 507 Calvin, K., Patel, P., Clarke, L., Asrar, G., Bond-Lamberty, B., Cui, R. Y., Di Vittorio, A., Dorheim, K.,  
508 Edmonds, J., and Hartin, C.: GCAM v5. 1: representing the linkages between energy, water, land, climate,  
509 and economic systems, *Geosci Model Dev*, 12, 677-698, 2019.
- 510 Chakraborty, T., Lee, X., and Lawrence, D. M.: Diffuse Radiation Forcing Constraints on Gross Primary  
511 Productivity and Global Terrestrial Evapotranspiration, *Earth's Future*, 10, e2022EF002805,  
512 <https://doi.org/10.1029/2022EF002805>, 2022a.
- 513 Chakraborty, T., Venter, Z., Qian, Y., and Lee, X.: Lower urban humidity moderates outdoor heat stress,  
514 *Agu Advances*, 3, e2022AV000729, 2022b.
- 515 Chakraborty, T. C., Lee, X., Ermida, S., and Zhan, W.: On the land emissivity assumption and Landsat-  
516 derived surface urban heat islands: A global analysis, *Remote Sens Environ*, 265, 112682,  
517 <https://doi.org/10.1016/j.rse.2021.112682>, 2021.
- 518 Chen, J., Qian, Y., Chakraborty, T., and Yang, Z.: Complexities of urban impacts on long-term seasonal  
519 trends in a mid-sized arid city, *Environmental Research Communications*, 2024.
- 520 Craig, A. P., Vertenstein, M., and Jacob, R.: A new flexible coupler for earth system modeling developed  
521 for CCSM4 and CESM1, *The International Journal of High Performance Computing Applications*, 26, 31-  
522 42, 2012.
- 523 Dai, Y., Zeng, X., Dickinson, R. E., Baker, I., Bonan, G. B., Bosilovich, M. G., Denning, A. S., Dirmeyer,  
524 P. A., Houser, P. R., Niu, G., Oleson, K. W., Schlosser, C. A., and Yang, Z.-L.: The Common Land Model,  
525 *B Am Meteorol Soc*, 84, 1013-1024, <https://doi.org/10.1175/BAMS-84-8-1013>, 2003.
- 526 Dickinson, R. E.: Modeling evapotranspiration for three-dimensional global climate models, *Climate*  
527 *processes and climate sensitivity*, 29, 58-72, 1984.
- 528 Fang, Y., Leung, L. R., Knox, R., Koven, C., and Bond-Lamberty, B.: Impact of the numerical solution  
529 approach of a plant hydrodynamic model (v0.1) on vegetation dynamics, *Geosci. Model Dev.*, 15, 6385-  
530 6398, 10.5194/gmd-15-6385-2022, 2022.
- 531 Fisher, R. A. and Koven, C. D.: Perspectives on the Future of Land Surface Models and the Challenges of  
532 Representing Complex Terrestrial Systems, *J Adv Model Earth Sy*, 12, e2018MS001453,  
533 <https://doi.org/10.1029/2018MS001453>, 2020.
- 534 Fisher, R. A., Muszala, S., Vertenstein, M., Lawrence, P., Xu, C., McDowell, N. G., Knox, R. G., Koven,  
535 C., Holm, J., and Rogers, B. M.: Taking off the training wheels: the properties of a dynamic vegetation  
536 model without climate envelopes, *CLM4. 5 (ED)*, *Geosci Model Dev*, 8, 3593-3619, 2015.





- 537 Gropp, W., Lusk, E., Doss, N., and Skjellum, A.: A high-performance, portable implementation of the MPI  
538 message passing interface standard, *Parallel Computing*, 22, 789-828, <https://doi.org/10.1016/0167->  
539 8191(96)00024-5, 1996.
- 540 Hao, D., Bisht, G., Gu, Y., Lee, W. L., Liou, K. N., and Leung, L. R.: A parameterization of sub-grid  
541 topographical effects on solar radiation in the E3SM Land Model (version 1.0): implementation and  
542 evaluation over the Tibetan Plateau, *Geosci. Model Dev.*, 14, 6273-6289, 10.5194/gmd-14-6273-2021,  
543 2021.
- 544 Hersbach, H., Bell, B., Berrisford, P., Hirahara, S., Horanyi, A., Muñoz-Sabater, J., Nicolas, J., Peubey, C.,  
545 Radu, R., Schepers, D., Simmons, A., Soci, C., Abdalla, S., Abellan, X., Balsamo, G., Bechtold, P., Biavati,  
546 G., Bidlot, J., Bonavita, M., De Chiara, G., Dahlgren, P., Dee, D., Diamantakis, M., Dragani, R., Flemming,  
547 J., Forbes, R., Fuentes, M., Geer, A., Haimberger, L., Healy, S., Hogan, R. J., Holm, E., Janiskova, M.,  
548 Keeley, S., Laloyaux, P., Lopez, P., Lupu, C., Radnoti, G., de Rosnay, P., Rozum, I., Vamborg, F., Villaume,  
549 S., and Thepaut, J. N.: The ERA5 global reanalysis, *Q J Roy Meteor Soc*, 146, 1999-2049, 10.1002/qj.3803,  
550 2020.
- 551 Hill, C., DeLuca, C., Suarez, M., and Da Silva, A.: The architecture of the earth system modeling framework,  
552 *Computing in Science & Engineering*, 6, 18-28, 2004.
- 553 Hong, S.-Y. and Lim, J.-O. J.: The WRF single-moment 6-class microphysics scheme (WSM6), *Asia-*  
554 *Pacific Journal of Atmospheric Sciences*, 42, 129-151, 2006.
- 555 Huang, H.: ELM code within WRF-ELM. Zenodo. <https://doi.org/10.5281/zenodo.11289807>, 2024
- 556 Huang, H., Xue, Y., Li, F., and Liu, Y.: Modeling long-term fire impact on ecosystem characteristics and  
557 surface energy using a process-based vegetation–fire model SSiB4/TRIFFID-Fire v1.0, *Geosci Model Dev*,  
558 13, 6029-6050, 10.5194/gmd-13-6029-2020, 2020a.
- 559 Huang, H., Xue, Y., Liu, Y., Li, F., and Okin, G. S.: Modeling the short-term fire effects on vegetation  
560 dynamics and surface energy in southern Africa using the improved SSiB4/TRIFFID-Fire model, *Geosci*  
561 *Model Dev*, 14, 7639-7657, 10.5194/gmd-14-7639-2021, 2021.
- 562 Huang, H., Xue, Y., Chilukoti, N., Liu, Y., Chen, G., and Diallo, I.: Assessing Global and Regional Effects  
563 of Reconstructed Land-Use and Land-Cover Change on Climate since 1950 Using a Coupled Land–  
564 Atmosphere–Ocean Model, *J Climate*, 33, 8997-9013, 10.1175/jcli-d-20-0108.1, 2020b.
- 565 Iacono, M. J., Delamere, J. S., Mlawer, E. J., Shephard, M. W., Clough, S. A., and Collins, W. D.: Radiative  
566 forcing by long-lived greenhouse gases: Calculations with the AER radiative transfer models, *Journal of*  
567 *Geophysical Research: Atmospheres*, 113, <https://doi.org/10.1029/2008JD009944>, 2008.
- 568 Jacob, R., Larson, J., and Ong, E.: M×N communication and parallel interpolation in Community Climate  
569 System Model Version 3 using the model coupling toolkit, *The International Journal of High Performance*  
570 *Computing Applications*, 19, 293-307, 2005.
- 571 Jenkinson, D. S.: The turnover of organic carbon and nitrogen in soil, *Philosophical Transactions of the*  
572 *Royal Society of London. Series B: Biological Sciences*, 329, 361-368, 1990.
- 573 Kayastha, M. B., Huang, C., Wang, J., Pringle, W. J., Chakraborty, T. C., Yang, Z., Hetland, R. D., Qian, Y.,  
574 and Xue, P.: Insights on Simulating Summer Warming of the Great Lakes: Understanding the Behavior of  
575 a Newly Developed Coupled Lake-Atmosphere Modeling System, *J Adv Model Earth Sy*, 15,  
576 e2023MS003620, <https://doi.org/10.1029/2023MS003620>, 2023.
- 577 Krayenhoff, E. S., Jiang, T., Christen, A., Martilli, A., Oke, T. R., Bailey, B. N., Nazarian, N., Voogt, J. A.,  
578 Giometto, M. G., and Stastny, A.: A multi-layer urban canopy meteorological model with trees (BEP-Tree):  
579 Street tree impacts on pedestrian-level climate, *Urban Climate*, 32, 100590, 2020.
- 580 Larson, J., Jacob, R., and Ong, E.: The model coupling toolkit: A new Fortran90 toolkit for building  
581 multiphysics parallel coupled models, *The International Journal of High Performance Computing*  
582 *Applications*, 19, 277-292, 2005.
- 583 Law, B.: Carbon dynamics in response to climate and disturbance: Recent progress from multi-scale  
584 measurements and modeling in AmeriFlux, *Plant responses to air pollution and global change*, 205-213,  
585 2005.
- 586 Lawrence, D. M., Fisher, R. A., Koven, C. D., Oleson, K. W., Swenson, S. C., Bonan, G., Collier, N.,  
587 Ghimire, B., van Kampenhou, L., Kennedy, D., Kluzek, E., Lawrence, P. J., Li, F., Li, H., Lombardo, Z.,



- 588 D., Riley, W. J., Sacks, W. J., Shi, M., Vertenstein, M., Wieder, W. R., Xu, C., Ali, A. A., Badger, A. M.,  
589 Bisht, G., van den Broeke, M., Brunke, M. A., Burns, S. P., Buzan, J., Clark, M., Craig, A., Dahlin, K.,  
590 Drewniak, B., Fisher, J. B., Flanner, M., Fox, A. M., Gentine, P., Hoffman, F., Keppel-Aleks, G., Knox, R.,  
591 Kumar, S., Lenaerts, J., Leung, L. R., Lipscomb, W. H., Lu, Y., Pandey, A., Pelletier, J. D., Perket, J.,  
592 Randerson, J. T., Ricciuto, D. M., Sanderson, B. M., Slater, A., Subin, Z. M., Tang, J., Thomas, R. Q., Val  
593 Martin, M., and Zeng, X.: The Community Land Model Version 5: Description of New Features,  
594 Benchmarking, and Impact of Forcing Uncertainty, *J Adv Model Earth Sy*, 11, 4245-4287,  
595 <https://doi.org/10.1029/2018MS001583>, 2019.
- 596 Li, C., Frolking, S., and Frolking, T. A.: A model of nitrous oxide evolution from soil driven by rainfall  
597 events: 1. Model structure and sensitivity, *Journal of Geophysical Research: Atmospheres*, 97, 9759-9776,  
598 1992.
- 599 Li, F., Zeng, X. D., and Levis, S.: A process-based fire parameterization of intermediate complexity in a  
600 Dynamic Global Vegetation Model, *Biogeosciences*, 9, 2761-2780, 10.5194/bg-9-2761-2012, 2012.
- 601 Li, L., Bisht, G., Hao, D., and Leung, L. R.: Global 1&thinsp;km land surface parameters for kilometer-  
602 scale Earth system modeling, *Earth Syst. Sci. Data*, 16, 2007-2032, 10.5194/essd-16-2007-2024, 2024.
- 603 Lin, Y. and Mitchell, K. E.: 1.2 the NCEP stage II/IV hourly precipitation analyses: Development and  
604 applications, *Proceedings of the 19th Conference Hydrology*, American Meteorological Society, San Diego,  
605 CA, USA,
- 606 Liu, Y., Xue, Y., MacDonald, G., Cox, P., and Zhang, Z.: Global vegetation variability and its response to  
607 elevated CO<sub>2</sub>, global warming, and climate variability – a study using the offline SSiB4/TRIFFID model  
608 and satellite data, *Earth Syst. Dynam.*, 10, 9-29, 10.5194/esd-10-9-2019, 2019.
- 609 Martín Belda, D., Anthoni, P., Wårlind, D., Olin, S., Schurgers, G., Tang, J., Smith, B., and Arneth, A.: LPJ-  
610 GUESS/LSMv1.0: a next-generation land surface model with high ecological realism, *Geosci. Model Dev.*,  
611 15, 6709-6745, 10.5194/gmd-15-6709-2022, 2022.
- 612 Muñoz-Sabater, J.: ERA5-Land monthly averaged data from 1950 to present., Copernicus Climate Change  
613 Service (C3S) Climate Data Store (CDS). [dataset], 10.24381/cds.68d2bb30, 2019.
- 614 Muñoz-Sabater, J., Dutra, E., Agustí-Panareda, A., Albergel, C., Arduini, G., Balsamo, G., Boussetta, S.,  
615 Choulga, M., Harrigan, S., Hersbach, H., Martens, B., Miralles, D. G., Piles, M., Rodríguez-Fernández, N.  
616 J., Zsoter, E., Buontempo, C., and Thépaut, J. N.: ERA5-Land: a state-of-the-art global reanalysis dataset  
617 for land applications, *Earth Syst. Sci. Data*, 13, 4349-4383, 10.5194/essd-13-4349-2021, 2021.
- 618 Nadolski, V.: Automated surface observing system user's guide, *NOAA Publ*, 12, 94, 1992.
- 619 Nelson, B. R., Prat, O. P., Seo, D. J., and Habib, E.: Assessment and Implications of NCEP Stage IV  
620 Quantitative Precipitation Estimates for Product Intercomparisons, *Weather and Forecasting*, 31, 371-394,  
621 <https://doi.org/10.1175/WAF-D-14-00112.1>, 2016.
- 622 Oleson, K. and Feddema, J.: Parameterization and surface data improvements and new capabilities for the  
623 Community Land Model Urban (CLMU), *J Adv Model Earth Sy*, 12, e2018MS001586, 2020.
- 624 Parton, W. J., Stewart, J. W., and Cole, C. V.: Dynamics of C, N, P and S in grassland soils: a model,  
625 *Biogeochemistry*, 5, 109-131, 1988.
- 626 Paschalis, A., Chakraborty, T., Fatichi, S., Meili, N., and Manoli, G.: Urban forests as main regulator of the  
627 evaporative cooling effect in cities, *AGU Advances*, 2, e2020AV000303, 2021.
- 628 Pelosi, A., Terribile, F., D'Urso, G., and Chirico, G. B.: Comparison of ERA5-Land and UERRA  
629 MESCAN-SURFEX reanalysis data with spatially interpolated weather observations for the regional  
630 assessment of reference evapotranspiration, *Water*, 12, 1669, 2020.
- 631 Qiu, H., Bisht, G., Li, L., Hao, D., and Xu, D.: Development of inter-grid-cell lateral unsaturated and  
632 saturated flow model in the E3SM Land Model (v2.0), *Geosci. Model Dev.*, 17, 143-167, 10.5194/gmd-17-  
633 143-2024, 2024.
- 634 Rizwan, A. M., Dennis, L. Y., and Chunho, L.: A review on the generation, determination and mitigation of  
635 Urban Heat Island, *Journal of environmental sciences*, 20, 120-128, 2008.
- 636 Schwab, D. J., Leshkevich, G. A., and Muhr, G. C.: Satellite Measurements of Surface Water Temperature  
637 in the Great Lakes: Great Lakes Coastwatch, *Journal of Great Lakes Research*, 18, 247-258,  
638 [https://doi.org/10.1016/S0380-1330\(92\)71292-1](https://doi.org/10.1016/S0380-1330(92)71292-1), 1992.





- 639 Sellers, P., Mintz, Y., Sud, Y. e. a., and Dalcher, A.: A simple biosphere model (SiB) for use within general  
640 circulation models, *J Atmos Sci*, 43, 505-531, 1986.
- 641 Sinha, E., Bond-Lamberty, B., Calvin, K. V., Drewniak, B. A., Bisht, G., Bernacchi, C., Blakely, B. J., and  
642 Moore, C. E.: The Impact of Crop Rotation and Spatially Varying Crop Parameters in the E3SM Land  
643 Model (ELMv2), *Journal of Geophysical Research: Biogeosciences*, 128, e2022JG007187, 2023.  
644 <https://doi.org/10.1029/2022JG007187>, 2023.
- 645 Skamarock, W. C. and Klemp, J. B.: A time-split nonhydrostatic atmospheric model for weather research  
646 and forecasting applications, *Journal of Computational Physics*, 227, 3465-3485,  
647 <https://doi.org/10.1016/j.jcp.2007.01.037>, 2008.
- 648 Soltani, A. and Sharifi, E.: Daily variation of urban heat island effect and its correlations to urban greenery:  
649 A case study of Adelaide, *Frontiers of Architectural Research*, 6, 529-538,  
650 <https://doi.org/10.1016/j.foar.2017.08.001>, 2017.
- 651 Stefanidis, K., Varlas, G., Vourka, A., Papadopoulos, A., and Dimitriou, E.: Delineating the relative  
652 contribution of climate related variables to chlorophyll-a and phytoplankton biomass in lakes using the  
653 ERA5-Land climate reanalysis data, *Water research*, 196, 117053, 2021.
- 654 Team, C. D.: ESCOMP/CTSM: release-clm5.0.37 (release-clm5.0.37) [dataset],  
655 <https://doi.org/10.5281/zenodo.11176755>, 2024.
- 656 Thompson, G., Rasmussen, R. M., and Manning, K.: Explicit Forecasts of Winter Precipitation Using an  
657 Improved Bulk Microphysics Scheme. Part I: Description and Sensitivity Analysis, *Mon Weather Rev*, 132,  
658 519-542, [https://doi.org/10.1175/1520-0493\(2004\)132<0519:EFOWPU>2.0.CO;2](https://doi.org/10.1175/1520-0493(2004)132<0519:EFOWPU>2.0.CO;2), 2004.
- 659 Thompson, G., Field, P. R., Rasmussen, R. M., and Hall, W. D.: Explicit Forecasts of Winter Precipitation  
660 Using an Improved Bulk Microphysics Scheme. Part II: Implementation of a New Snow Parameterization,  
661 *Mon Weather Rev*, 136, 5095-5115, <https://doi.org/10.1175/2008MWR2387.1>, 2008.
- 662 Thonicke, K., Spessa, A., Prentice, I. C., Harrison, S. P., Dong, L., and Carmona-Moreno, C.: The influence  
663 of vegetation, fire spread and fire behaviour on biomass burning and trace gas emissions: results from a  
664 process-based model (vol 7, pg 1991, 2010), *Biogeosciences*, 7, 2191-2191, 10.5194/bg-7-2191-2010, 2010.
- 665 Thornton, M., Shrestha, R., Wei, Y., Thornton, P., Kao, S., and Wilson, B.: Daymet: Daily Surface Weather  
666 Data on a 1-km Grid for North America, Version 4 R1. ORNL DAAC, Oak Ridge, Tennessee, USA.,  
667 <https://doi.org/10.3334/ORNLDAAC/2129>, 2022.
- 668 UCAR: Using CTSM with WRF — CTSM documentation., <https://escomp.github.io/ctsm-docs/versions/master/html/lilac/specific-atm-models/wrf.html>, 2020.
- 670 Wang, J., Xue, P., Pringle, W., Yang, Z., and Qian, Y.: Impacts of Lake Surface Temperature on the Summer  
671 Climate Over the Great Lakes Region, *Journal of Geophysical Research: Atmospheres*, 127,  
672 e2021JD036231, <https://doi.org/10.1029/2021JD036231>, 2022a.
- 673 Wang, J., Qian, Y., Pringle, W., Chakraborty, T. C., Hetland, R., Yang, Z., and Xue, P.: Contrasting effects  
674 of lake breeze and urbanization on heat stress in Chicago metropolitan area, *Urban Climate*, 48, 101429,  
675 <https://doi.org/10.1016/j.uclim.2023.101429>, 2023.
- 676 Wang, Y.-R., Hessen, D. O., Samset, B. H., and Stordal, F.: Evaluating global and regional land warming  
677 trends in the past decades with both MODIS and ERA5-Land land surface temperature data, *Remote Sens*  
678 *Environ*, 280, 113181, <https://doi.org/10.1016/j.rse.2022.113181>, 2022b.
- 679 Weng, E., Malyshev, S., Lichstein, J., Farrior, C. E., Dyzbinski, R., Zhang, T., Shevliakova, E., and Pacala,  
680 S. W.: Scaling from individual trees to forests in an Earth system modeling framework using a  
681 mathematically tractable model of height-structured competition, *Biogeosciences*, 12, 2655-2694, 2015.
- 682 Wiltshire, A. J., Duran Rojas, M. C., Edwards, J. M., Gedney, N., Harper, A. B., Hartley, A. J., Hendry, M.  
683 A., Robertson, E., and Smout-Day, K.: JULES-GL7: the Global Land configuration of the Joint UK Land  
684 Environment Simulator version 7.0 and 7.2, *Geosci. Model Dev.*, 13, 483-505, 10.5194/gmd-13-483-2020,  
685 2020.
- 686 Xia, Y., Mitchell, K., Ek, M., Sheffield, J., Cosgrove, B., Wood, E., Luo, L., Alonge, C., Wei, H., Meng, J.,  
687 Livneh, B., Lettenmaier, D., Koren, V., Duan, Q., Mo, K., Fan, Y., and Mocko, D.: Continental-scale water  
688 and energy flux analysis and validation for the North American Land Data Assimilation System project



689 phase 2 (NLDAS-2): 1. Intercomparison and application of model products, *Journal of Geophysical*  
690 *Research: Atmospheres*, 117, <https://doi.org/10.1029/2011JD016048>, 2012.  
691 Xu, C., Christoffersen, B., Robbins, Z., Knox, R., Fisher, R. A., Chitra-Tarak, R., Slot, M., Solander, K.,  
692 Kueppers, L., Koven, C., and McDowell, N.: Quantification of hydraulic trait control on plant  
693 hydrodynamics and risk of hydraulic failure within a demographic structured vegetation model in a tropical  
694 forest (FATES–HYDRO V1.0), *Geosci. Model Dev.*, 16, 6267–6283, [10.5194/gmd-16-6267-2023](https://doi.org/10.5194/gmd-16-6267-2023), 2023.  
695 Xue, Y., Sellers, P. J., Kinter, J. L., and Shukla, J.: A Simplified Biosphere Model for Global Climate Studies,  
696 *J Climate*, 4, 345–364, [https://doi.org/10.1175/1520-0442\(1991\)004<0345:ASBMFG>2.0.CO;2](https://doi.org/10.1175/1520-0442(1991)004<0345:ASBMFG>2.0.CO;2), 1991.  
697 Yuan, F., Wang, D., Kao, S.-C., Thornton, M., Ricciuto, D., Salmon, V., Iversen, C., Schwartz, P., and  
698 Thornton, P.: An ultrahigh-resolution E3SM land model simulation framework and its first application to  
699 the Seward Peninsula in Alaska, *Journal of Computational Science*, 73, 102145, 2023.

700